ACS OMEGA

http://pubs.acs.org/journal/acsodf

Article

Microfluidic Study of the Electrocoalescence of Aqueous Droplets in Crude Oil

Thomas Leary, Mohsen Yeganeh, and Charles Maldarelli*

Cite This: *ACS Omega* 2020, 5, 7348−7360

Read Online

ACCESS | Metrics & More | Article Recommendations | Supporting Information

ABSTRACT: In electrocoalescence, an electric field is applied to a dispersion of conducting water droplets in a poorly conducting oil to force the droplets to merge in the direction of the field. Electrocoalescence is used in petroleum refining to separate water from crude oil and in droplet-based microfluidics to combine droplets of water in oil and to break emulsions. Using a microfluidic design to generate a two-dimensional (2D) emulsion, we demonstrate that electrocoalescence in an opaque crude oil can be visualized with optical microscopy and studied on an individual droplet basis in a chamber whose height is small enough to make the dispersions two dimensional and transparent. From reconstructions of images of the 2D electrocoalescence, the electrostatic forces driving the droplet merging are calculated in a numerically exact manner and used to predict observed coalescence events. Hence, the direct simulation of the electrocoalescence-driven breakdown of 2D emulsions in microfluidic devices can be envisioned.

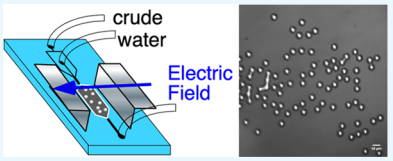

1. INTRODUCTION

Electric field-mediated coalescence of conducting water droplets dispersed in a continuous, poorly conducting dielectric oil phase (Figure 1) is a long-standing technology

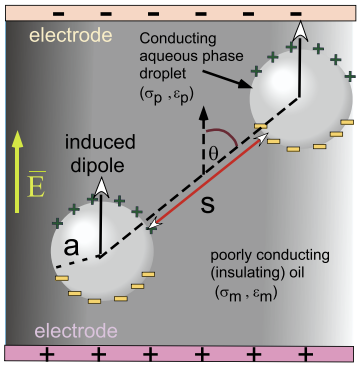

Figure 1. Induced dipole formation on the surfaces of a pair of spherical conducting aqueous droplets in a poorly conducting oil phase due to an imposed uniform electric field $\bar{E}$ and the dipole−dipole interaction between the droplets, which creates an interdroplet attractive force.

in the petroleum refining industry. This technology has been used to remove emulsion droplets of water in crude oil,[1−7] particularly in the context of the desalting operation of electrocoalescers. In this operation, fresh water is first introduced into the crude at the inlet to the electrocoalescer to remove organic salts by transferring into the water phase. The introduction of the water creates an emulsion of the water in oil, which is passed between electrodes. The electric field between the electrodes coalesces the salt-laden droplets in the direction of the field. Successive coalescence events between droplets produce progressively larger droplets that settle under gravity into a bulk water phase that can be easily removed. Generally, these water in crude oil emulsions are strongly stabilized against coalescence by the adsorption onto the water/oil interface of surface-active components from the oil, particularly the alkylated, polyaromatic asphaltenes (for reviews, see Mullins et al.[8−10]). Asphaltenes adsorb onto the interface to form interfacial layers, which in time age and give rise to highly elastic skins that resist droplet coalescence under typical conditions (for reviews, see refs 11, 12 and the studies[13−18]). In an electrocoalescer, these highly stabilized droplets are forced to merge at sufficiently high electric field strengths. Despite the importance of the electrocoalescence process in the refining industry, the fundamentals of this phenomenon are still evolving. This is in part due to the difficulty of examination of electrocoalescence in crudes because of the oil opacity. Therefore, many studies thus far substitute oil with a clean, transparent fluid that may not reproduce the crude oil environment, e.g., refs 19−23.

Microfluidics can enable a direct visualization of electrocoalescence in crudes by generating emulsions in which the droplets are arranged in a single layer with a small depth transparent to optical microscopy, e.g., refs 24, 25. Microfluidics also offers the ability to form emulsions of controlled and uniform size (e.g., through the use of "T" junctions, flow-focusing orifices, and capillary tips).[26−29] The first goal of this

Received: December 12, 2019
Accepted: March 2, 2020
Published: March 23, 2020

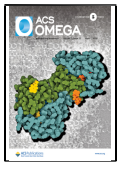

https://dx.doi.org/10.1021/acsomega.9b04259
ACS Omega 2020, 5, 7348−7360

study is to demonstrate these unique fluid handling and visualization capabilities of microfluidics using crude oil to demonstrate how the electrocoalesence process in crudes can be examined in situ using microfluidics.

More recently, interest in electrocoalesence has focused on lab on chip devices[30−40] in which two-dimensional (2D) water-in-oil emulsions are used for chemical or biological assays, extractions, and separations. In this context, electrocoalescence has drawn interest as a means for combining droplets and breaking water-in-oil emulsions to complete the chip operations (see for example[41−50]). As explained below, the model problem of the electrocoalescence of droplet pairs has been theoretically and experimentally examined as in Figure 1. However, few studies have examined theoretically the dynamics of electrocoalescence of emulsions in which the breakdown process is determined by multiple attractive and repulsive forces exerted on each droplet. This multidroplet process underlies the breakdown of water-in-crude oil emulsions and the combining of droplets and the breakdown of emulsions on lab on-chip processes. The second goal of this study is to obtain theoretical solutions for the electric field in the continuous phase of a microfluidically generated uniform 2D emulsion to predict electrocoalescence forces and coalescence events and to compare these predictions with the experiments.

In this study, we use a microfluidic arrangement to generate a train of water droplets in a continuous crude oil phase in a channel. The train is directed to a wide chamber in which the droplets are arranged in a single layer lubricated from above and below by very thin layers of oil. We term this freely moving, two-dimensional assembly a "2D emulsion". We apply an electric field along the layer to cause the droplets to merge and the emulsion to breakdown. Numerical configurations of droplet arrangements in this 2D emulsion are reconstructed from images of electrocoalescence experiments in a microfluidic chamber. The electrical forces exerted on the droplets are computed to predict merging events. These predictions coincide with the merging events observed in the experiment, suggesting the breakdown can be simulated and potentially programmed, and this is the second motivation of our study.

We begin with a brief review. Electrocoalescence of an isolated pair of droplets of water in a continuous oil under a uniform applied electric field, Figure 1, has been studied theoretically[22,51−68] and experimentally.[19−22,62,68−77] The electrohydrodynamic forces, which cause the droplets to merge in the direction of the field, have been described by the field-induced charge distribution on the surface of the droplets. For an isolated spherical water droplet of radius a placed in a uniform oscillating field ($\overline{E}\, e^{i\omega t}$ where $\overline{E}$ is the amplitude, t is the time, and ω is the frequency), mobile ions in the water and possibly oil phases are conducted in the field direction. In electrocoalesence, the conductivities and dielectric constants of the droplet phase, σ_p and ε_p, are larger than those of the oil continuous phase, σ_m and ε_m. Therefore, free and bound positive (negative) charges accumulate at the side of the droplet facing (opposite) to the direction of the electric field. To leading order, an oscillating electric dipole aligned with the field, $\mathcal{P}(t)$, is induced as given by[78−81] $\mathcal{P}(t) = 4\pi\varepsilon_o\varepsilon_m a^3 \mathcal{R}e[\mathcal{F}_{CM}\overline{E}\ e^{i\omega t}]$. Here, $\mathcal{R}e$ denotes the real part of the bracketed expression, $\mathcal{F}_{CM} = \frac{\varepsilon_p^* - \varepsilon_m^*}{\varepsilon_p^* + 2\varepsilon_m^*}$ is the Clausius Mossotti factor defined in terms of the complex dielectric constants of the oil and water phases with $\varepsilon_p^* = \varepsilon_o\varepsilon_p - \frac{i\sigma_p}{\omega}$ and $\varepsilon_m^* = \varepsilon_o\varepsilon_m - \frac{i\sigma_m}{\omega}$, and ε_o is the permittivity of free space. Typically, $\sigma_p \gg \sigma_m$ and $\varepsilon_p \gg \varepsilon_m$, and hence, $\mathcal{F}_{CM} = 1$. For a droplet pair, interaction forces arise principally because the dipole induced on each of the droplets falls within the dipole electric field created by its neighbor. For spherical droplets, the interaction depends on the angle of orientation of the droplet pair axis with the field, θ, and the edge-to-edge separation distance, s (Figure 1). If the electric field acting on each droplet is approximated by the far field dipole field of its neighbor, then the time average pairwise interaction force along the centerline is[19−21,82]

$$\frac{\langle \mathcal{F}_r(t)\rangle}{\varepsilon_o\varepsilon_m a^2 \overline{E}_{RMS}^2} = 12\pi \frac{|\mathcal{F}_{CM}|^2(1 - 3\cos^2\theta)}{\left(2 + \frac{s}{a}\right)^4} \quad (1)$$

where $\overline{E}_{RMS}$, the root mean square of the oscillating field, is equal to $\overline{E}/\sqrt{2}$. The dipole field of the neighbor and correspondingly the force on the droplet intensify as the droplets approach one another. When the droplets are aligned with the field, $\theta = 0$, the force is attractive as dipoles line-up end-to-end. Whereas, when the droplets are alongside each other, $\theta = \pi/2$, the force is repulsive as the dipoles are parallel. Exact solutions for the interaction force between spherical conductors in a perfectly insulating dielectric ($\mathcal{F}_{CM} = 1$) subject to a uniform electric field are obtained by Davis[83] using bispherical coordinates. For $\theta = 0$, the interaction force is written in terms of the nondimensional function $\mathfrak{F}(s/a)$, i.e., $\frac{\langle \mathcal{F}_r(t)\rangle}{\varepsilon_o\varepsilon_m a^2 \overline{E}_{RMS}^2} = -\mathfrak{F}(s/a)$. The bispherical exact solution for the force demonstrates that the dipole approximation is valid for $s/a > 1$, but the exact solution increases much more rapidly than the dipole approximation for $s/a < 1$. For $10^{-3} < s/a < 10^{-1}$, a numerical fit[22] is $\mathfrak{F}(s/a) \approx 0.92\pi\left\{\frac{a}{s}\right\}^{0.8}$. For $\theta = 0$, the bispherical solution shows that the maximum value of the electric field is at the poles of the droplets facing each other and is given by $\overline{E}\mathcal{G}(s/a)$. This can be approximated as[22,59] $\mathcal{G}(s/a) \approx 1.87\left\{\frac{a}{s}\right\}^{0.85}$ for $10^{-3} < s/a < 10^{-1}$.

For a single aqueous droplet in oil subject to a uniform field (e.g., refs 53, 84−86), the applied field exerts an electrical normal traction (Maxwell stress) on the induced free or bound surface charge. This, in turn, causes the droplets to deform in the field direction as prolate figures, which adopt conical tips ("Taylor" cones) at higher field strengths before bursting. This deformation scales as the electrocapillary number $E_c = \frac{\varepsilon_o\varepsilon_m\overline{E}^2 a}{\gamma}$ where γ is the interfacial tension. For isolated droplet pairs approaching each other due to dipolar attraction and small $E_c \ll 1$, the droplets remain spherical for $s/a > 1$. Assuming spherical shapes ($E_c \ll 1$) and balancing the dipolar interaction force and viscous resistance with the lubrication theory for close enough separations (typically inertial forces are negligible), Eow et al.[19] and Chiesa et al.[20,21] compute trajectories starting from large separation distances $s/a > 1$ and up to coalescence. Their results agree well with corresponding experimental trajectories. More recent studies[58,60−62,66,67,77] account for interface deformation and again map successfully theoretical predictions with experimental results on the

https://dx.doi.org/10.1021/acsomega.9b04259
ACS Omega 2020, 5, 7348−7360

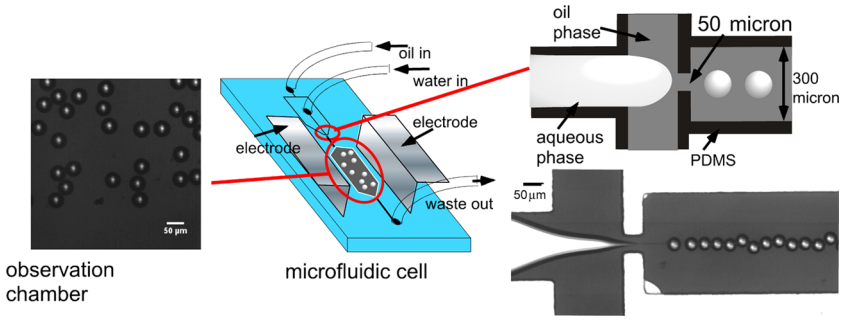

Figure 2. Schematic of the microfluidic cell including the arrangement of the flow-focusing orifice to form individual droplets and the chamber in which the droplets assemble into a 2D emulsion and the electric field is applied. Shown also are images of the drop generation at the orifice (the schematic and the frame from the video) and the 2D emulsion in the chamber (the frame from the video). The scale bars are 50 μm.

trajectories of droplet pairs driven together by electrocoalescence.

The details of the final stages of electrocoalescence as the droplets approach to within a few tenths of a radius of each other and merge are more complicated. The merging process takes place on time scales of tens of milliseconds, which are typically much shorter than the time scale for the approach of droplets. As relatively spherical droplets approach ($E_c \ll 1$) one another, the electric field exerted on the facing poles intensifies, and pronounced opposing prolate deformations develop that precede coalescence. These deformations have been examined theoretically by accounting for interface deformation in continuum computational simulations[61−66] and molecular dynamics simulations.[68]

The final stages in the electrocoalescence process have also been visualized in small fluidic cells or microfluidic arrangements in which, in a continuous oil phase, an electric field is applied across free aqueous droplet pairs along their line of centers[70−74] or anchored droplets at a fixed potential difference are arranged to face one another.[75,87−94] The dynamics are visualized over a time interval of hundreds of milliseconds from an initial separation distance s_o/a. Three regimes are recognized: (i) no coalescence due to a large gap distance or a too small field strength, (ii) coalescence at large enough field strengths, or (iii) partial coalescence and repulsion at typically larger field strengths than necessary for coalescence. Coalescence is observed as a liquid bridge forms between the droplets from their individual prolate deformations. The liquid bridge then grows in radius to the order of the droplet radii bringing the droplets together into one fluid mass. In partial coalescence, the facing droplet interfaces are deformed into cones that connect to form a narrow bridge that becomes unstable, breaks, and drives a recoil. In the case of coalescence, which is of interest here, for anchored droplets at fixed potentials, Atten et al.[89] measured the critical potential difference V_{crit} at which the droplet faces merge. They correlated their results as the critical electrical capillary number $\frac{\varepsilon_o \varepsilon_m a}{\gamma}\frac{V_{crit}^2}{s_o^2}$ as a function of $s_o/a < 1$ and find critical capillary numbers in the range of 0.2−0.4. These values agreed with their numerical calculations and are in the range of other theoretical calculations of anchored or suspended droplets in close proximity ($s_o/a < 1$), e.g., Latham and Roxburgh,[51] Taylor,[52] and Atten.[59]

The dynamics of electrocoalescence of multiple water droplets in water-in-oil emulsions has only been examined recently by Garstecki et al.[95] They generated a 2D emulsion with flow focusing of water and hexadecane in a microfluidic cell and observed electrocoalescence across the emulsion under an AC field. They find a critical field strength necessary for electrocoalescence, which decreases with decreasing ω and increasing σ_p. This suggests that the faster the free charge relaxation in the water droplet phase (time scale $\frac{\varepsilon_o \varepsilon_p}{\sigma_p}$) relative to the AC oscillation ($1/\omega$), the greater is the charge separation (dipole strength) for an applied field. This is due to a redistribution of more free charge on the surface and higher droplet polarization, resulting in a greater dipolar attraction.

2. RESULTS AND DISCUSSION

2.1. Visualization of Electrocoalesence in Crudes in a Microfluidic Cell. Our microfluidic experiments on the visualization of electrocoalescence of water droplets in an opaque petroleum crude are undertaken in a polydimethylsiloxane (PDMS) transparent cell using flow focusing at an orifice to form water droplets in the crude in a channel as a droplet train and directing the train to a wide chamber in which an AC field is applied to the 2D emulsion, which forms cf. Figure 2. (The fabrication of the cell, the material properties of the crude (including the dynamic oil/water tension), and the details of the applied field and frequency are described in the Experimental Section.) Figure 2 shows the flow-focusing production of the water droplets in oil at the orifice and the 2D emulsion of the droplets in the chamber prior to the application of the field. As is clear from the images, the droplets in the crude (which appears opaque and black in a 10 mL test tube) are readily visualized in the microfluidic cell due to the small thickness of the optical slice (60 μm). The droplets are monodisperse in size with a diameter of $2a$ = 36−48 μm. The assembled 2D emulsion presents interdroplet distances s, which vary from under one droplet diameter to several diameters. The separation distances are quantified when the droplet configuration is rendered for numerical calculation of the electric field and interdroplet forces. Under most circumstances in the flow-focusing generation of water drops in oil, surfactants are required in the oil phase to reduce the oil/water tension. This is necessary so that the water phase, drawn into a thread in the orifice, breaks into droplets.[96] Here, the surface-active molecules native to the crude (e.g., asphaltenes) serve this role, and importantly, electrocoalescence of water droplets in crude can be examined in situ without any additional surfactants. The naturally reduced interfacial tensions of crudes against water (here 28 mN/m, Figure 8 in Experimental Section) allow a large deformability

https://dx.doi.org/10.1021/acsomega.9b04259
ACS Omega 2020, 5, 7348−7360

of the interface, ensuring that the water is easily segmented into drops at the flow-focusing orifice.

Figure 3 shows an illustrative sequence of images of electrocoalescence events in the chamber, over a period of

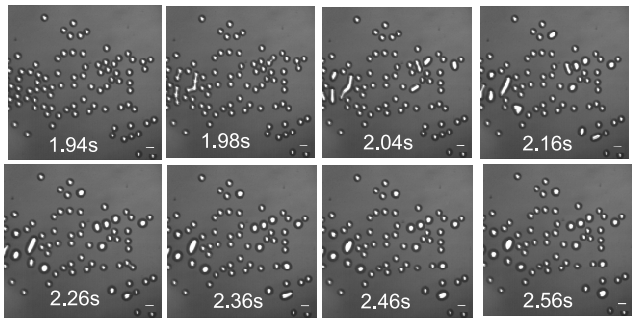

Figure 3. Image sequence of the electrocoalescence of droplets in the chamber at times of 1.94−2.56 s, referenced from the moment (t = 0) the field is energized. In the first configuration, at 1.94 s, no droplets have yet coalesced. The scale bar is 50 μm. The field is applied top-to-bottom with $\mathcal{E}_{electrode}$ = 250 V/mm.

approximately 1/2 s, for a field strength $\mathcal{E}_{electrode}$ = 250 V/mm. The images are a bird's eye view of the 2D emulsion, with the field applied top-to-bottom, and with the assigned times relative to the moment the field is energized (the video is available in the Supporting Information.) For the first image shown in the sequence, no coalescence events have occurred. The sequence in Figure 3 includes droplet pairs coalescing, as well as events in which groups of three and four droplets coalesce. Also evident (the lower right-hand side of the figure) is a cascading event where two droplets merge, and the combined drop merges with a neighbor brought closer due to the prior electrocoalescence event as also observed by Garstecki et al.[95] The coalescence events are clearly between droplets close enough so that they are a few tenths of a radius apart. Typically, coalescing droplets are aligned closely with the field. For an isolated pair of droplets, the dipole interaction force predicts an attractive force for $0 < \theta < \theta_c$ where θ_c is given by $3\cos^2\theta_c - 1 = 0$, cf. eq (1), and is equal to 54.8°. For all of the coalescence events in Figure 3, the angle between the field and the line of centers between the droplet pair falls between 0 and approximately 55° in agreement with the dipole force approximation. Droplet pairs with angles larger than approximately 55° do not coalesce, even at close separation distance. Isolated droplet pairs that merge follow a common pattern in which they deform toward each other to create a joining liquid bridge (Figure 3). The faces of each drop, which are opposite to the bridging thread, remain more spherical as the field has not intensified on those surfaces away from the region between the drops. The connecting thread increases in radius until the drops merge and readopt a spherical configuration. While the coalescence process itself takes place on a time scale of milliseconds, the equilibration to a spherical shape takes place on a time scale of hundreds of milliseconds to 1 s. The triple droplet and quadruple droplet merging evident in the sequence of Figure 3 appear as simultaneous events between the multiple droplets. In these cases, connecting liquid threads form between adjoining pairs to form a merged cylinder that eventually relaxes to a spherical shape. Qualitatively, over the time frame studied, the coalescence events appear without noticeable movement of the droplets toward each other. Critical fields required for the coalescence of droplets a few tenths of a radius close to one another appear to be reached, and the droplets coalesce in place.

2.2. Theoretical Calculation of Electric Field in the 2D Emulsion. Figure 3 makes clear that, upon application of the electric field, the electrocoalescence events in the crude oil can be recognized, cataloged, and sequenced. We demonstrate that these events can also be predicted by first computing the electric field distribution in the emulsion and then evaluating the field at the surfaces of the droplets to calculate the interdroplet forces and identify pairwise attractive interactions leading to the merging of droplet pairs. For a given droplet in the emulsion, the electric field that is experienced is determined by the imposed far field and by the droplets around them, and therefore the computation of the field is a mulitibody calculation. We use COMSOL Multiphysics 4.2 to obtain a numerical finite element solution for the electric field in the continuous oil phase. We start with an image captured at the beginning of an experiment in which the field has been turned on, but no coalescence has occurred (e.g., the first image of Figure 3). We render the two-dimensional images, representing the instantaneous configuration of uncoalesced droplets, into a three-dimensional (3D) COMSOL computational domain. This is intended to reproduce the observation chamber and the arrangements of droplets in the chamber. The droplets are modeled as fluid spheres and positioned in the computational domain at their exact locations in the image. The locations of the perimeters of the droplets in the 2D images are obtained by edge detection. The intensity range of each pixel is 0−255, and the perimeter is located by identifying the change in pixel intensity from bright (within the droplets) to dark (the exterior crude oil) along directions approximately perpendicular to the perimeter. The change occurs over the order of a few pixels, and the perimeter is demarcated as a set of points at which the area under the intensity vs pixel position on either side of a given point (relative to the asymptotic values on either side) is equal. Using this algorithm, the edge is located to an error of approximately one-half of a pixel or half a micron. The points are then fit to a circle with a radius, which is assigned to the radius of the droplet at that point. The center of the circle is assigned the center location of the droplet. A sphere is constructed from that center with the assigned radius and positioned halfway between the top and bottom of the chamber. The domain height is set equal to the chamber height $\mathcal{H}$ = 60 μm, and the domain width ($\mathcal{W}^*$ = 1 mm) and length ($\mathcal{L}^*$=1 mm section) are set equal to the width of the chamber and the length observed in the captured image. The top and bottom are maintained at a potential difference $\mathcal{V}_{chamber}$, which is computed from the driving potential difference applied across the electrodes inserted into the PDMS ($\mathcal{V}_{electrode}$). Values of the dielectric constant of the cured PDMS elastomer (2.0)[97] are approximately equal to the measured dielectric constant of the crude (2.5). Hence, for the purposes of the calculation of $\mathcal{V}_{chamber}$, the PDMS and crude in the chamber are considered as perfect dielectrics in capacitive series, leading to $\frac{\mathcal{V}_{chamber}}{\mathcal{W}} = \frac{\mathcal{V}_{electrode}}{2l_c + \mathcal{W}}$, which in the experiments is equal to 250 V/mm. Although the droplets settle downward during their residence time in the chamber, the approximation that they are at the center of the chamber for the electrostatic calculation is valid because the dielectric constants of the PDMS and oil are nearly equal. The applied potential is 0 V on the bottom, −250

https://dx.doi.org/10.1021/acsomega.9b04259
ACS Omega 2020, 5, 7348−7360

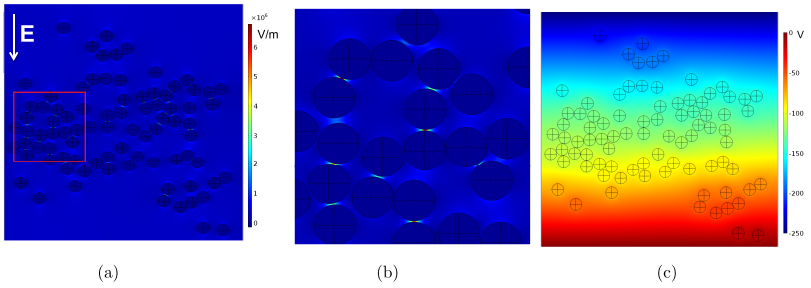

Figure 4. (a) Rendering of the COMSOL computational domain for the configuration of droplets in the 2D emulsion subject to a uniform field (up-to-down) as depicted in the image of Figure 2 at 1.94 s, prior to electrocoalescence events. Also shown is a superposition of the magnitude of the electric field (in the uniform field direction) in the oil and droplet phases. (b) Color map of the magnitude of the electric field for the inset region shown in (a). (c) Color map of the electrostatic potential around the droplets for the scale as in (a).

$V = \mathcal{V}_{\text{chamber}}$ on the top. This is corresponding to the experimental gradient of 250 V/mm with the electric field directed from top to bottom. As the potentials are fixed, the calculations are undertaken assuming a static DC field is applied. As we demonstrate below, the equations and solutions for the electric field are all quasi-static. Hence from these solutions, to obtain the forces on the droplets to compare to the AC experiments, the square of the DC field strength used in the force calculations ($\frac{\mathcal{V}^2_{\text{chamber}}}{\mathcal{W}^2}$) is replaced by 1/2 the square of the field, corresponding to the time average of the 250 V/mm AC field in the experiments.

To calculate the electric field, the crude, a poor conductor, is modeled as a "leaky dielectric"[98] with zero volume charge density. This satisfies $\nabla^2\phi_m = 0$, where ϕ_m is the oil electrostatic potential (made dimensionless with $\mathcal{V}_{\text{chamber}}$) and formulated in COMSOL's cartesian coordinate representation of the computational domain. Each of the $\mathcal{N}$ spheres in the computation domain is modeled as ohmic conductors in which the volume free charge relaxes quickly relative to $1/\omega$ (i.e., $\Omega > 1$). Therefore, the potential field in the spheres is quasi-static and satisfies $\nabla^2\phi_{p(i)} = 0$, $i = 1,..\mathcal{N}$ where $\phi_{p(i)}$ is the nondimensional electrostatic potential within drop i. The boundary conditions on the surface of each of the spheres are continuity of the electric potential, $\phi_m = \phi_{p(i)}$, $(i = 1, 2..\mathcal{N})$ and the surface charge density conditions, $\varepsilon^*\frac{\partial\rho_{s(i)}}{\partial\tau} = \Omega\mathbf{n}_i\cdot\{\nabla\phi_{p(i)} - \sigma^*\nabla\phi_{m(i)}\}$ (charge balance) and $\varepsilon^*\rho_{s(i)} = \mathbf{n}_i\cdot\{\varepsilon^*\nabla\phi_m - \nabla\phi_{p(i)}\}$ (Gauss's law). Here, $\mathbf{n}_i$ is the unit outward normal to the sphere i and τ is the time nondimensionalized by $1/\omega$ and $\rho_{s(i)}$ is the surface charge density on droplet i nondimensionalized by $\varepsilon_o\varepsilon_m\mathcal{V}_{\text{chamber}}/\mathcal{W}$. $\sigma^* = \frac{\sigma_m}{\sigma_p} = 10^{-3}$ and $\varepsilon^* = \frac{\varepsilon_m}{\varepsilon_p} = 0.03$ are, respectively, the ratios of the conductivities and dielectric constants of the continuous crude oil to the aqueous droplet phase. For Ω large and ϵ^* small, the surface charge balance becomes quasi-static: $\mathbf{n}_i\cdot\nabla\phi_{p(i)} = \sigma^*\mathbf{n}_i\cdot\nabla\phi_m$. We use this quasi-static formulation for the charge balance to obtain the potential fields, which are thereby quasi-static. In fact, since $\sigma^* \ll 1$, this quasi-static balance reduces to $\mathbf{n}_i\cdot\nabla\phi_{p(i)} \approx 0$, which requires the electrostatic field in each of the droplets to be equal to zero and the droplets to be at uniform (though different) nondimensional potentials $\mathcal{V}_i$. The problem could be solved by computing the potential in the oil outside of the droplets subject to these constant potential conditions, but the potentials would have to be obtained by requiring zero charge on each of the droplets. Here, we retain the quasi-static surface charge balance at the droplet interfaces, using the measured values of the conductivities and dielectric constants for the simulation, and solve for the potentials within each drop as well as in the oil. In this way, the surface charge density can later be computed from $\rho_{s(i)} = \left\{1 - \frac{\sigma^*}{\varepsilon^*}\right\}\mathbf{n}_i\cdot\nabla\phi_m$. This charge density would automatically satisfy zero net charge on each droplet interface since from the charge balance $\int_{\mathcal{A}_i}\rho_{s(i)}d\mathcal{A} = \{1 - \sigma^*/\varepsilon^*\}\int_{\mathcal{A}_i}\mathbf{n}_i\cdot\nabla\phi_m d\mathcal{A} = \left\{\frac{1}{\sigma^*} - \frac{1}{\varepsilon^*}\right\}\int_{\mathcal{A}_i}\mathbf{n}_i\cdot\nabla\phi_{p,i}d\mathcal{A} = 0$. Here, $\mathcal{A}_i$ is the nondimensional area of droplet i scaled by a^2 and the last equality follows because the droplet potential fields satisfy Laplace's equation. The three-dimensional simulation domain is then closed by side walls in which the potential in the oil has assumed to relax. We also require $\mathbf{n}_w\cdot\nabla\phi_m = 0$ where $\mathbf{n}_w$ is the unit outward normal to the side walls. To validate the calculations, we first compute the electric field and the electrocoalescence force between a droplet pair aligned with the field, see the Theoretical Calculation of Electric Field in the 2D Emulsion Section.

Figure 4a shows the COMSOL computational domain reproducing the configuration of the droplets in the 2D emulsion in Figure 3 for a time of 1.94 s, which is prior to any coalescence events. The figure also shows an overlay of a color map of the magnitude of the electric field in the droplets and continuous oil phase in the direction of the applied field. Although the field details are course, the enhanced electric fields between close droplet pairs whose center-to-center axes are approximately aligned with the applied field are clear. In comparison, the fields between droplet pairs aligned perpendicular to the field, even when they are very close together, are not as intensified. This can be understood if we consider, to a first approximation, the electric field between the droplets to be a superposition of the uniform far field and the dipolar fields generated by the dipoles created on the two droplets of the pair by the uniform field. Again to a first approximation, the droplet dipoles (Figure 1) lie in the uniform field direction. Each dipole field is strongest at the poles and weakest at the equator, and hence, the electric field is much larger in gaps between droplet pairs aligned with the uniform field. The electric fields within the droplets are zero. More details are provided in Figure 4b, which shows the electric field in the smaller region of the emulsion boxed in red in Figure 4a and in Figure 4c, which shows the electric potential of the larger region. Figure 4b clearly indicates the

https://dx.doi.org/10.1021/acsomega.9b04259
ACS Omega 2020, 5, 7348−7360

intensification of field strength between droplets aligned with the field. Note from the color map that the field is of order 5.0−7.5 × 10^6 V/m between the closest droplets aligned with the field. This is approximately 20−30 times the applied gradient of 2.5 × 10^5 V/m. The potential distribution, however, indicates that, for a given droplet pair, the dipolar fields generated from the assemblage of neighboring droplets also affect the field between the pair. The droplets are at uniform (though different) potentials as is clear from the color map of Figure 4c. Consequently, groups of droplets with uniform potentials within their interiors attenuate the up-down potential gradient imposed by the electrodes. This is clearly evident in the transverse zones of nearly uniform color in Figure 4c that widen as they envelop groups of droplets. If the conductivities of the droplets were equal to that of the oil, the applied potential gradient would be unattenuated, and the potential field would consist of straight, parallel stripes transversing the domain. The attenuation of the applied field and the local change in the gradient of the potential from the strictly up-down direction imposed by the electrodes affect the polarization of the droplets and the intensity and orientation of the dipoles induced on the droplets. Changes in dipolar intensity and direction affect the interdroplet forces and the pattern of droplet electrocoalescence.

2.3. Theoretical Calculation of Electrocoalescence Forces. From the finite element simulations of the quasi-static electric field around the droplets in their arrangement in the 2D emulsion, the electrical forces on each of the droplets can be computed. This provides a detailed understanding and prediction of the coalescence events. We consider precoalescence arrangements at 1.94 s (i.e., Figure 3) and predict the merging events for $t > 1.94$ s. Excepting coalescence events, the fluids in the continuous and droplet phases are relatively static. The hydrodynamic stresses due to the flow recirculation move droplets relative to one another. However, Figure 3 indicates that this drifting does not move the droplets appreciably over the half-second of the duration of the sequence. (As the drift velocity is of order 20 μm/s, this short time period would correspond to (1/2) of a radius in movement.) In our consideration of the coalescence events, we only examine a window of 100 ms from an observed configuration prior to any coalescence (e.g., the first three snapshots in Figure 3). We therefore neglect the slow flow as the integrated effects of the hydrodynamic drift forces are negligible. For the static arrangement, the oil phase is only subject to the nondimensional pressure p_m, scaled by $\varepsilon_o\left\{\frac{\mathcal{V}_{chamber}}{\mathcal{W}}\right\}^2$, and the force of the field on the polarization charge $\mathbf{P}_m\cdot\nabla\mathbf{E}_m = (1/2)(\varepsilon_m - 1)\nabla\{|\mathbf{E}_m|^2\}$. Here, $\mathbf{E}_m = -\nabla\phi_m$ is the nondimensional electric field scaled by $\left\{\frac{\mathcal{V}_{chamber}}{\mathcal{W}}\right\}$ and $\mathbf{P}_m$ is the nondimensional polarization in the oil. The pressure is given by $-p_m = C - \frac{1}{2}(\varepsilon_m - 1)|\mathbf{E}_m|^2$ where C is a constant. The dimensionless force on droplet i, $\mathbf{F}_i$, scaled by $\varepsilon_o\varepsilon_m a^2\left\{\frac{\mathcal{V}_{chamber}}{\mathcal{W}}\right\}^2$, is the integration of the dimensionless Maxwell tension, $\mathbf{T}_m = \varepsilon_m\mathbf{E}_m\mathbf{E}_m - (1/2)|\mathbf{E}_m|^2\mathbf{I}$, and the pressure, where $\mathbf{I}$ is the unit tensor. Thus, $\mathbf{F}_i = \int_{\mathcal{A}_i}\{-p_m\mathbf{n}_i + \mathbf{n}_i\cdot\mathbf{T}_m\}d\mathcal{A} = \frac{1}{2}\int_{\mathcal{A}_i}|\mathbf{n}_i\cdot\mathbf{E}_m|^2\mathbf{n}_i d\mathcal{A}$ where the contribution of the tangential component of the electric field is neglected due to the high conductivity of the aqueous phase relative to the oil.

For a pairwise set of droplets (i, j) we compute the nondimensional interdroplet interaction force as $F_{i,j} = \hat{\mathbf{r}}_{i,j}\cdot\{\mathbf{F}_j - \mathbf{F}_i\}$. Here, $\hat{\mathbf{r}}_{i,j}$ is the unit vector extending from droplet i to droplet j in the field. As shown in Figure 5a, for droplets "1" and "2" with dimensionless position vectors $\mathbf{r}_1$ and $\mathbf{r}_2$ (scaled by a) from an origin and forces $\mathbf{F}_1$ and $\mathbf{F}_2$, $\hat{r}_{1,2} = \frac{\mathbf{r}_2 - \mathbf{r}_1}{|\mathbf{r}_2 - \mathbf{r}_1|}$. With this definition, negative values of $F_{i,j}$ indicate attraction between the pair along their line of centers and positive values repulsion. Each droplet only has a certain number of nearest neighbors, which block its potential coalescence with other droplets. Therefore, an algorithm is employed to identify which droplet pairs are not obstructed by a third droplet and are potentially able to coalescence. For example (Figure 5b), droplet 2 is an accessible neighbor of droplet 1 if the distance d from droplet "3" center to the line of centers from droplet 1 to droplet 2 is greater than the radius of droplet 3.

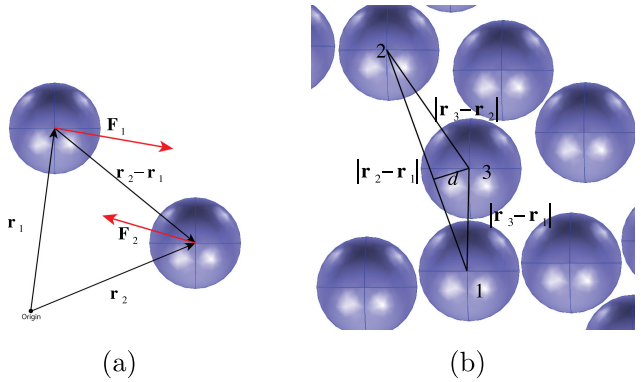

Figure 5. (a) Position and force vectors for defining the interdroplet force and (b) algorithm for identifying accessible neighbors.

Using these calculations, in Figure 6, the instantaneous normalized, nondimensional force $\tilde{F}_{i,j}$ between pairs of droplets (i, j) of accessible neighbors acquired from captured images is plotted as a function of the pair separation distance, s/a. Circles denote the fate of the pair over the following 100 ms, i.e., coalescence (red) or noncoalescence (blue). Figure 6 displays the results of six sets of experiments, of which Figure 3

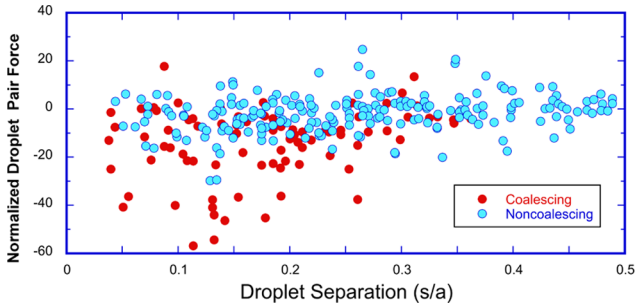

Figure 6. Plot of instantaneous normalized nondimensional electrostatic force, $\tilde{F}_{i,j}$ calculated between droplet pairs in 2D emulsion configurations as obtained from captured images taken prior to any coalescence. The nondimensional force $\tilde{F}_{i,j}$ is scaled by the Davis[83] calculation of the force between a droplet pair aligned with the field and at one radius separation, i.e., $\tilde{F}_{i,j} = \hat{r}_{i,j}\cdot\{\mathbf{F}_j - \mathbf{F}_i\}/\mathfrak{F}(s/a = 1)$. Filled red (blue) circles indicate droplet pairs that coalesce (do not coalesce) over an interval of 100 ms from the time that the image configuration on which the forces are computed is taken.

https://dx.doi.org/10.1021/acsomega.9b04259
ACS Omega 2020, 5, 7348−7360

represents one set, with approximately 60−80 droplets in each set, and with all drops considered in the simulation. The total number of droplet pairs accessible for coalescence, which are reported in Figure 6, is 288 with 84 pairs coalescing. In Figure 6, the nondimensional force is scaled by the force between two isolated droplets, which are subject to, and aligned with, a uniform field $(\frac{\mathcal{V}_{\text{chamber}}}{\mathcal{W}})$ at one radius of separation as computed by Davis;[83] thus $\tilde{F}_{i,j} = \hat{r}_{i,j}\cdot\{\mathbf{F}_j - \mathbf{F}_i\}/\mathfrak{F}(s/a = 1)$. The dimensional interdroplet force is therefore given by $\frac{1}{2}\tilde{F}_{i,j}\varepsilon_o\varepsilon_m a^2\left\{\frac{\mathcal{V}_{\text{chamber}}}{\mathcal{W}}\right\}^2\mathfrak{F}(s/a = 1)$. The factor of 1/2 accounting for the AC applied field.

The interdroplet separation distances s/a plotted in Figure 6 are between 0.05 and 0.5. Separation distances s/a from 0.5 to about 2 are observed, but these typically correspond to pairs in which coalescence is not possible because of intervening neighbors (Figure 5b). For separations larger than approximately two with no intervening neighbors are present, but they are too far to coalesce in the 100 ms of observation from the frame capture. We also note that the shortest edge-to-edge separation distance observed in the plot is 0.05, which approaches the limit of the accuracy in the detection of the droplet edge (0.025).

Figure 6 makes clear that large normalized, nondimensional attractive forces, from −20 to −40, develop between the droplets for separation $s/a < 0.25$. This is as expected, since for the two-droplet problem, drops aligned with the field can, for $0.05 < s/a < 0.25$, develop attractive forces 10 to 100 times the force at one radius of separation (the normalizing value in Figure 6). (See Figure 9 and the Atten et al.[22] fit $\mathfrak{F}(s/a) \approx -0.92\pi\left\{\frac{a}{s}\right\}^{0.8}$ for the two-droplet forces.) For larger values of the separation distance $(0.5 > s/a > 0.25)$, the attractive forces drop off dramatically to the range of $-10 < \tilde{F}_{i,j} < 0$. This is also expected due to the significant reduction in the dipolar force (Figure 9a). Repulsive forces $(\tilde{F}_{i,j} > 0)$ are small over the entire range of separation distances, of order 1−10. This is also in agreement with the repulsive interaction force between two droplets aligned perpendicular to the field, where the repulsive force in magnitude is 0.1.[83] The calculated larger repulsive values are due to the attractive interaction forces of neighboring droplets on the droplet pair, which act to push the droplets away from each other.

From Figure 6, an assessment can be made on whether droplet pairs, which are calculated to be attractive in the instantaneous configuration in the images, do in fact coalesce in the 100 ms following the image capture. The figure indicates that almost all of the droplets with the largest attraction, $|\tilde{F}_{i,j}| > 20$, which fall in the range $s/a < 0.25$, do coalesce. This is made clearer in a histogram plot, Figure 7a, of the count of the number of pairs, which coalesce (or do not coalesce), binned as a function of the normalized droplet pair force, $|\tilde{F}_{i,j}| > 20$. The reason that the few pairs (3, cf. Figure 7a) that do not coalesce is the fact that one member of the pair coalesced with a member of another pair. However, less than half of the droplet pairs with smaller computed attractive forces, $|\tilde{F}_{i,j}| < 20$, coalesces, even when the distance of separation is small $(0.05 < s/a < 0.35)$. Pairs with even smaller attractions $(|\tilde{F}_{i,j}| < 10)$ and greater separations $(0.35 < s/a < 0.5)$ do not coalesce at all.

To understand these results, we note that a coalescence event occurs as droplet pairs approach to a critical distance where the field strength is large enough that droplets deform

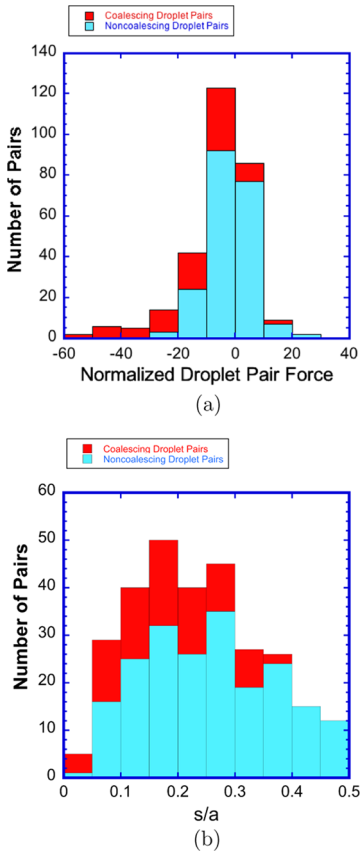

Figure 7. Histograms of the number of droplet pairs that coalesce or do not coalesce binned as a function of (a) normalized pairwise force $\tilde{F}_{i,j}$ and (b) separation distance s/a.

significantly and join through a liquid bridge, as seen in Figure 3. For the instantaneous configurations on which the normalized attractive and repulsive forces are calculated, the measured separation distances that are plotted are small $(0.05 < s_o/a < 0.5)$. Coalescence is achieved as long as the droplet pair, either initially or within the 100 ms of observation, comes to a separation distance such that the critical field strength (which is a function of the dipoles of its neighbors) for coalescence is reached. To predict coalescence, we can use the results on the merging of anchored droplets. As reviewed in the introduction, in these studies (Atten et al.[89]), anchored, facing droplets are held at a fixed potential difference V and positioned at initial separation distances $10^{-3} < s_o/a < 1$. The droplets deform and are found to merge when the imposed potential difference V exceeds a critical value V_{crit}. The merging occurs at a critical distance, s_{crit}/a, which is approximately 0.6 s_o/a. At this critical distance, the Maxwell tensions exerted by the normal electric field strengths at the facing poles are large enough that equilibrium solutions for prolate shapes no longer exist and droplets merge. This critical potential difference is correlated in terms of a critical electrocapillary number, which can be defined in terms of the electric field strength at the facing poles of the droplet pair at the coalescence point, i.e., $E_{\text{c,crit}} = \frac{\varepsilon_o\varepsilon_m a}{\gamma}\frac{V_{\text{crit}}^2}{s_{\text{crit}}^2}$. This is equal to 0.2−0.4, depending on the initial separation and the size of the capillary tips anchoring the droplets to the droplet radii.

With the above as context, consider first the droplet pairs with a large net attractive force, $|\tilde{F}_{i,j}| > 20$ $(s_o/a < 0.25)$. By

https://dx.doi.org/10.1021/acsomega.9b04259
ACS Omega 2020, 5, 7348−7360

examining the droplet pairs in this class, we observe that in most cases, the pair is aligned along the field (or close to this orientation) and at a short enough separation distance, so that the electric field at the facing poles is large. In addition, in these cases, the neighbors are either located at a far enough distance that they do not interact with the pair in the calculation of the interdroplet force or are arranged around the droplet pair perpendicular to the field so that only small repulsive forces are exerted. In these cases, the field at the poles is large enough that the critical capillary number is exceeded and the droplets coalesce. From the color map in Figure 4b as an example and using the exact calculations, we find that the droplets with large net attractive force ($|\tilde{F}_{i,j}| > 20$) have electric fields at their facing poles, which are 20−30 terms larger than the applied field strength. The electrocapillary number corresponding to the applied field strength of 250 V/mm and γ = 28 mN/m (the value of the dynamic tension at the residence time for the droplets in the wide chamber) is equal to $E_c = \frac{\varepsilon_o \varepsilon_m \bar{E}^2_{RMS} a}{\gamma} = 5 \times 10^{-4}$ (using the RMS value for the field). The droplets with large attractive force $|\tilde{F}_{i,j}| > 20$ (separations $s/a < 0.25$ and electric field amplification of 20−30 the applied strength) have electrocapillary numbers in the range of 0.2−0.45. This is in the interval for coalescence and explains why they coalesce. It is also important to note that the electrocapillary numbers, at the point of coalescence with amplification of the fields, are still relatively small. Therefore, the droplets remain spherical until the point of coalescence, as is evident in the images of Figure 3a,b, and this is true in all of the remaining cases discussed below. The classes of droplets in Figure 6 with very small mutual attraction forces $|\tilde{F}_{i,j}| < 10$ and large separations $0.35 < s/a < 0.5$, on examination, have electric field values at their poles less than 10 times the applied strength. This leads to electrocapillary numbers no greater than 0.05, insufficient for coalescence.

In the class of droplets in Figure 6 with small attractive forces $|\tilde{F}_{i,j}| <20$ for $s/a < 0.35$, some merge and some do not. An examination of the pairs in this category shows that the ones that do not merge have field amplification at the poles, which are smaller than 10, and hence electrocapillary numbers below the range required for coalescence. The ones that do merge have the requisite amplification, though, interestingly their attractive force is not as large as the droplets in the class where $|\tilde{F}_{i,j}| > 20$. Case by case examination shows the coalescing pairs have neighbors in the field direction, which are close enough to exert attractive forces that reduce the net attractive interdroplet force between the pair. Thus, droplets can merge even if the attraction is not large. For this same reason, the few droplets pairs with net repulsion, which do merge in Figure 6 on examination, have bounding neighbors in the field direction that exert strong attractions on the pair members. This provides a resulting net repulsion between the members, even though the field on the facing surfaces of the droplets of the pair is large enough for coalescence. The above analysis of the criteria for electrocoalescence does not take into account the effect of the asphaltene film on the droplet interface on the coalescence. When an asphaltene film is present with a large surface elasticity, the elastic forces contribute to the restoring effects. This phenomenon acts against the Maxwell stress, and thus the restoring forces due to the tension are not the only surface restoring forces. The dynamics of the interface for this case has not been studied in detail, but a starting point would be to assume an equation of state for the tension, which would include the elastic effect due to the stretching of the asphaltene film. Following Rane et al.,[17] we could start with their supposition that the Langmuir equation of state is valid, $\gamma(\Gamma) = \gamma_o + RT\Gamma_\infty \ln\left\{1 - \frac{\Gamma}{\Gamma_\infty}\right\}$ where Γ is the surface concentration of the asphaltene, Γ_∞ is the maximum packing concentration of the asphaltene, and γ_o is the tension in the absence of asphaltenes. As the area of the interface changes during electrocoalescence, the surface concentration changes. If we assume no additional adsorption during the time scale of the electrocoalescence process, then the surface concentration is given by the conservation equation, and the area expansion represents the strain on the film. For this case, the elasticity of the layer, which would account for the surface film, is $E_o(\Gamma_o) = -\Gamma_o\left[\frac{\partial \gamma}{\partial \Gamma}\right]_{\Gamma=\Gamma_o}$ where Γ_o is the asphaltene concentration at the point in which the field is applied. Following in this way, two nondimensional groups would appear. The first group is the electrocapillary number and a second group ($E_E = \frac{\varepsilon_o \varepsilon_m \bar{E}^2 a}{E_o(\Gamma_o)}$) corresponding to the ratio of the Maxwell stress to the film elasticity. Note that in this formulation, the surface concentration Γ_o is directly related to the aging. For electrocoalesence, these ratios should exceed critical values. We note that other elastomechanical expressions could be formulated instead of the Langmuir equation of state, but in all cases, a second group would appear representing a value for the characteristic Maxwell stress to the characteristic film elasticity. Rane et al.[17] undertake measurements of the film elasticity by oscillating a pendant drop and find that E_o increases with the age of the drop, with values between 0 and 30 mN/m for aging between 0 and 120 min. Hence, the elasticity is of the order of the tension. In our analysis, we base our criteria for electrocoalescence on the values of E_c, stating that when E_c is large enough, electrocoalescence occurs as the Mawell stresses are sufficiently larger than the tension. Since the elasticity is the same order as the tension, if Maxwell stresses are sufficiently large to exceed the restoring force of tension, the same should be true for the restoring force of elasticity. If the interfacial tension is extremely low (<1mN/m), then the dominant effect would be the elastic resistance. Alternatively, if the droplets are only aged a short amount of time, the elasticity is very low and the dominant effect is the tension.

3. CONCLUSIONS

This study has examined the process of electrocoalescence in a 2D emulsion of conducting water droplets in an insulating oil phase, which is generated in a microfluidic cell. An electric field applied across the emulsion induces charge separation and dipole formation in the conducting water droplets. The polarized droplets attract each other through dipolar forces, which intensify as the droplets approach to within a few tenths of a radius of each other. Petroleum crude is used for the oil because of the important applications of electrocoalescence to the removal of water from the crude. However, current interest is focused on the "droplet-based" microfluidic lab on chip applications that use electrocoalescence to combine droplets and break emulsions. Our microfluidic design uses flow focusing of water in oil to generate water droplets of uniform size, which are guided downstream as a single layer into a wide observation chamber. The 2D emulsion forms as the droplets

https://dx.doi.org/10.1021/acsomega.9b04259
ACS Omega 2020, 5, 7348−7360

collect in the chamber and an electric field is applied across the chamber to induce electrocoalescence. Our study provides two unique contributions: We demonstrate that our microfluidic design enables the electrocoalescence process in an opaque continuous phase to be visualized on the scale of the droplets with optical microscopy because the narrow chamber height allows the emulsion to become transparent. Electrocoalescence events are observed on an individual droplet basis, allowing an in situ examination of the merging process. Our study also demonstrates that the droplet scale data can be modeled to identify critical conditions for electrocoalescence using a local electrocapillary number. Numerical simulations for the electric field around the droplets in 2D configurations rendered directly from frame captures of microscopy images are obtained and used to compute the forces on the droplets. From the calculated forces, the mutual forces of attraction (or repulsion) between droplet pairs in the rendered images are examined as a function of the pair separation distance. These calculations are correlated with whether the droplet pair coalesced in the short (100 ms) time interval that followed from the captured frame on which the force calculation was based. Large mutual attractive forces at small separations (a few tenths of a droplet radius) correlated to electrocoalescence of the pair as the electric field between the droplets exceeded the value necessary for coalescence. Larger separations (approximately one-half of a radius) and very small attractive (or repulsive) forces correlated to noncoalescing droplets as the electric field strengths are too low. Almost all droplet pairs with repulsive interactions did not coalesce. For droplet pairs at close separation (a few tenths of a droplet radius) and intermediate values for mutual attraction, some pairs coalesced and some did not. An examination of the electric field on the droplet surfaces showed that for droplet pairs in this class that did coalesce the field strength between the droplets became large enough for coalescence. However, the net forces on each of the droplets (and hence the mutual force of attraction) were reduced because of the attractive interactions with neighboring droplets. Our demonstration that the electric field in a 2D emulsion can be computed exactly from rendered images and used to correlate coalescence events allows for a more in-depth study of the factors affecting electrocoalesence. This can open the possibility of programming the electrocoalesence process by manipulation of the applied electric field. Our approach of simulating directly the multiple droplet electrocoalescence to identify critical field strengths is also applicable to a three-dimensional study, although the visualization of the droplets in 3D would require other techniques such as pulsed field gradient (PFG) NMR since the 3D crude would be opaque in a microfluidic arrangement in which the channel height was larger to accommodate a 3D dispersion of droplets. The use of PFG-NMR to study water in crude oil emulsions has been undertaken by Sjoblom et al.[99−101]

4. EXPERIMENTAL SECTION

A petroleum crude (ExxonMobil) with $\varepsilon_m = 2.5$ and $\sigma_m = 1.1 \times 10^{-8}$ S/m (measured by an impedance analyzer, Agilent), viscosity $\mu_m = 0.023$ kg m^{-1} s^{-1} (cone and plate viscometer), and density $\rho_m = 8.75 \times 10^2$ kg/m^3 is used, and the aqueous droplet phase is DI water with an assumed ε_p of 80, a measured σ_p of 1.2×10^{-5} S/m (conductivity meter), and $\rho_p = 1.0 \times 10^3$ kg/m^3. The crude oil/DI water dynamic interfacial tension, γ, is measured using a pendant drop tensiometer (Kruss) and is shown in Figure 8. (All data at 20 °C, the temperature of

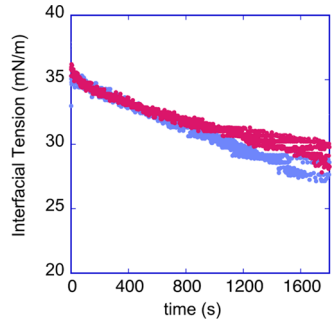

Figure 8. Dynamic interfacial tension between a crude oil droplet and DI water over a period of 2000 s; the graph shows three realizations.

experiments). The asphaltene content of the crude was obtained by extraction of the asphaltene with heptane (see e.g., ref 9 ASTM 863-69 standard), and the asphaltene content was 0.5 percent by weight and visually the crude appeared opaque.

The microfluidic cell is made using soft lithography[102] and fabrication of two layers of polymerized and cured PDMS. One layer containing the open fluidic channels and chamber inscribed on one face is molded by curing PDMS (Sylgard 184, Dow Corning) over a negative epoxy master of the fluidic features. The second is a flat layer to seal the channel. The two layers are bonded together following exposure to an oxygen plasma and mounted on a standard glass microscope slide. Access ports cored into the top layer using a biopsy punch allow the introduction of the oil and aqueous streams via polyethylene tubing (1.5 mm OD) inserted into the ports and connected to syringe pumps (Harvard Apparatus PHD). The exit port allows the emulsion to exit through inserted tubing. A monodisperse train of water droplets suspended in the crude is generated by flow-focusing streams of crude and water through separate channels from entry ports to an orifice where the droplets are formed. The train is directed through a feeding channel to a holding chamber (width $\mathcal{W} = 3$ mm and length $\mathcal{L} = 10$ mm) in which the droplets arrange themselves in an arbitrary configuration to form the 2D emulsion, and in which the electric field is applied. Droplets leave the chamber through an exiting channel ending in an exit port. Feeding and exit channel widths to the chamber are 300 μm and 2 mm long, and the height of the channels and chamber is $\mathcal{H} = 60$ μm, which (see below) is small enough for the crude to be transparent. The flow-focusing orifice is 50 μm in width, and at the flow rates of oil and water used ($q_m = 0.2$ μL/min and $q_p = 0.02$ μL/min, respectively), droplets approximately 40 μm in diameter are generated. The droplets move through the feeding channel and the chamber as a single layer. For the field generation, planar electrodes of aluminum are inserted through the cell, perpendicular to its lateral plane, and sited parallel to the chamber at a distance l_c. The electrodes were connected to an amplifier (TeK) controlled by a frequency generator (Agilent), which applied a potential $\mathcal{E}_{electrode}$ across the electrodes. To prevent accumulation of charge and reduction of field strength, a sinusoidal AC rather than a DC driving potential is applied across the electrodes. The applied field is oscillated at a frequency $\omega = 500$ Hz so that $\Omega = \frac{\sigma_p}{\varepsilon_o \varepsilon_p \omega} = 4.5$ and the free volume charge in the conducting aqueous phase relaxes quickly relative to the inverse of the frequency. Droplet coalescence events in the chamber are visualized by optical

https://dx.doi.org/10.1021/acsomega.9b04259
ACS Omega 2020, 5, 7348−7360

microscopy using a microscope (Nikon) in the bright-field mode and recorded with a high-speed camera (Redlake, 50 frames/s) with a 10×, N.A. 1.4 (air) objective. The sensor has a pixel area of 1280 × 1024, and the field of view in the observation cell was 1 mm × 1 mm or a resolution of approximately 1 μm per pixel.

The experiments are undertaken in a continuous flow-through mode. The width of the chamber in the microfluidics device is much larger than the width of the microchannel, which feeds the droplets into the chamber. Therefore, the droplet movement in the chamber is relatively slow, and the droplets appear to drift very slowly across the field of view. At the oil flow rate q_m used, the characteristic velocity of the droplets in the channel is $q_m/(\mathcal{H}\times 300\mu\text{m}) \approx 200\ \mu$m/s and in the chamber is $\langle v\rangle = q_m/(\mathcal{H}\times\mathcal{W}) \approx 20\mu$m/s. In the absence of an applied field, a steady state is established, the field is then energized for a few seconds, and a video of the coalescence dynamics in the chamber is recorded from the moment the potential is applied. The field is then turned off, and the slow flow in the chamber flushes the coalesced drops out. The experiment is then repeated after microscopy observation reveals there are no coalesced droplets in the chamber. Thus, for the droplets observed in the chamber during an experiment, the approximate time between their formation at the orifice and the initiation of the field is approximately 500 s ($\mathcal{L}/\langle v\rangle$) as the residence time of the droplets in the channel feeding the chamber is only approximately 10 s ($2\times 10^3\ \mu$m/200 μm/s). This 500 s time represents the approximate "aging time" of the droplets from their formation at the flow-focusing orifice. This time is important in applying the results of this microfluidic electrocoalescence study to the operation of field electro-coalescers. The residence time of the droplets in the electrocoalescer from their point of formation is important as it determines how long asphaltenes (and other surface-active material in the oil) have been allowed to adsorb from the oil onto the droplet surface. As we noted in the introduction, the greater this aging time the more elastic the interfacial layer and the more difficult it becomes for the droplets to merge. Conventional coalescers operate with a residences time of 30–40 min[103] to deliver production rates of tens to hundreds of kilobarrales of oil/day. Newer compact designs, which have improved the efficiency of the electrocoalescence process, operate with lower holding volumes that have reduced this residence time.[6,7] The residence times of 10 min in our experiments are of the order of the times for more compact electrocoalescers, so our study reflects realistic conditions. More importantly, the aging time can be increased (or adjusted to a desired value) within our microfluidic chip design by using longer, serpentine-shaped channels feeding into the chamber as undertaken by Nowbahar et al.[24]

5. COMPUTATIONAL METHODS

To validate the COMSOL calculation of the electrostatic field in the 2D emulsion of multiple water droplets in oil and the calculations of the forces on the droplets, we first simulate the electric field between two equally sized spherical droplets (radius $a = 20\ \mu$m). The simulation is carried out for droplets in our computational chamber with the center-to-center axis between the droplets perpendicular to the top and bottom walls on which the potential difference $\mathcal{V}_{\text{chamber}}$ is applied. The bounding surfaces of the chamber are set to be far from the droplet pair ($\mathcal{H} = \mathcal{W} = \mathcal{L} = 10a$). This represents the condition of a uniform electric field applied at infinity to two isolated drops, as solved by Davis[83] analytically using bispherical coordinates. In Figure 9, we provide a color map

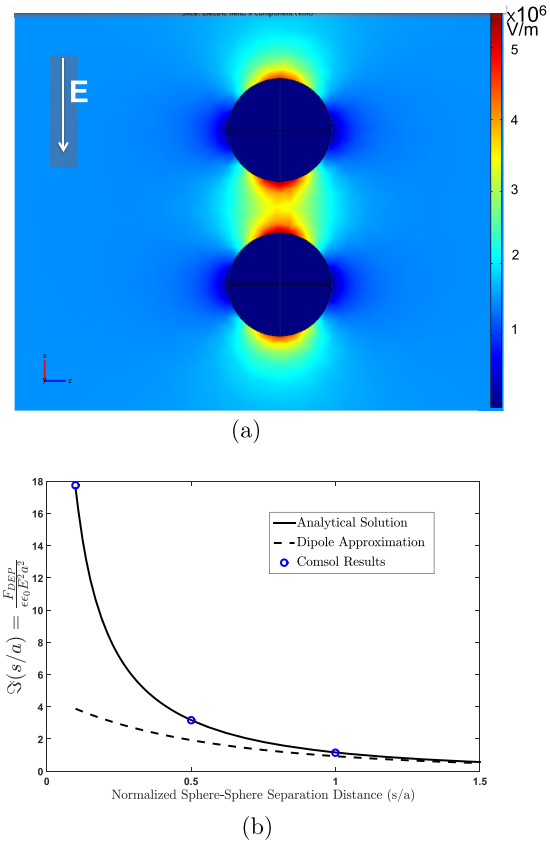

Figure 9. (a) Pair of isolated droplets aligned with a uniform electric field applied far away (up-to-down) and a color map of the electric field in the uniform field direction as computed numerically (COMSOL). (b) The nondimensionalized attractive force $\mathfrak{F}(s/a)$ exerted on each of the pairs as a function of the edge-to-edge separation s/a as computed from the COMSOL simulation and the bispherical analytical solution[83] and compared to the dipole approximation.

of the field strength in a slice perpendicular to the top and bottom of the chamber. It contains the equatorial planes of both droplets for the conductivity and viscosity ratios of our multidroplet water-in-oil simulations ($\sigma^* = 10^{-3}$, $\varepsilon^* = 0.03$). Since the droplets are so much more conductive than the oil, their electric fields are essentially zero in the droplets, as evident from the map. The intensification of the field between the droplets, which is the driving force of the electro-coalescence, is apparent with the highest field strengths at the poles of the facing droplets. Quantitatively, we obtain the attractive electrical force between the droplets, scaled by $\varepsilon_o\varepsilon_m a^2\frac{\mathcal{V}^2_{\text{chamber}}}{\mathcal{W}^2}$, (denoted by $\mathfrak{F}(s/a)$ as in the introduction) through the integration of the normal electric field on the surface of the droplets. This force is compared in Figure 9 with the exact analytical solution obtained by Davis.[83] The agreement is excellent, demonstrating that because of the very low conductivity ratio of the oil to the water droplet phase, the field is essentially that of a continuous phase. The agreement also provides confidence in our COMSOL solutions

https://dx.doi.org/10.1021/acsomega.9b04259
ACS Omega 2020, 5, 7348−7360

for the multidroplet simulations. We also note that the dipole−dipole approximation for the force is satisfactory for interdroplet separations s/a larger than one.

■ ASSOCIATED CONTENT

Supporting Information

The Supporting Information is available free of charge at https://pubs.acs.org/doi/10.1021/acsomega.9b04259.

AVI video of electrocoalesence corresponding to Figure 3 (AVI)

■ AUTHOR INFORMATION

Corresponding Author

Charles Maldarelli − *The Benjamin Levich Institute for Physicochemical Hydrodynamics and Department of Chemical Engineering, The City College of New York, New York, New York 10031, United States;* orcid.org/0000-0001-7427-2349; Email: cmaldarelli@ccny.cuny.edu

Authors

Thomas Leary − *The Benjamin Levich Institute for Physicochemical Hydrodynamics and Department of Chemical Engineering, The City College of New York, New York, New York 10031, United States*

Mohsen Yeganeh − *ExxonMobil Research and Engineering Company, Annandale, New Jersey 08801, United States*

Complete contact information is available at: https://pubs.acs.org/10.1021/acsomega.9b04259

Notes

The authors declare no competing financial interest.

■ ACKNOWLEDGMENTS

This work was partially supported by an NSF grant to the Center for the Exploitation of Nanostructures in Sensors and Energy Systems (CENSES), an Army Research Office grant ARO W911NF-11-1-0161, the Donors of the American Chemical Society Petroleum Research Fund, and ExxonMobil Research and Engineering Co.

■ REFERENCES

(1) Waterman, L. Electrocoalescers. *Chem. Eng. Prog.* **1965**, *61*, 51−57.

(2) Galvin, C. Design principles for electrocoalescers. *IChemE Symp. Ser.* **1986**, *88*, 101−113.

(3) Eow, J.; Ghadiri, M.; Sharif, A.; Williams, T. Electrostatic enhancement of coalecence of water droplets in oil: A review of the current understanding. *Chem. Eng. J.* **2001**, *84*, 173−192.

(4) Eow, J.; Gadhiri, M. Electrostatic enhancement of coalescence of water droplets in oil: a review of the technology. *Chem. Eng. J.* **2002**, *85*, 357−368.

(5) Lundgaard, L.; Berg, G.; Ingebrigtsen, S.; Atten, P. *Emulsions and Emulsion Stability*; Sjoblom, J., Ed.; Taylor and Francis, 2006; pp 549−592.

(6) Less, S.; Vilagines, R. The electrocoalescers' technology: Advances, strengths and limitations for crude oil separation. *J. Pet. Sci. Eng.* **2012**, *81*, 57−63.

(7) Mhatre, S.; Vivacquaa, V.; Ghadiri, M.; Abdullaha, A.; Al-Marri, M.; Hassanpour, A.; Hewakandamby, B.; Azzopardi, B.; Kermani, B. Electrostatic phase separation: a review. *Chem. Eng. Res. Des.* **2015**, *96*, 177−195.

(8) Mullins, O. C. Review of the molecular structure and aggregation of asphaltenes and petroleomics. *SPE J.* **2008**, *13*, 48−57.

(9) Mullins, O. C. The asphaltenes. *Ann. Rev. Anal. Chem.* **2011**, *4*, 393−418.

(10) Mullins, O. C.; Sabbah, H.; Eyssautier, J.; Pomerantz, A. E.; Barré, L.; Andrews, A. B.; Ruiz-Morales, Y.; Mostowfi, F.; McFarlane, R.; Goual, L. Advances in asphaltene science and the Yen-Mullins model. *Energy Fuels* **2012**, *26*, 3986−4003.

(11) McLean, J. D.; Spiecker, P. M.; Sullivan, A. P.; Kilpatrick, P. K. *Structures and Dynamics of Asphaltenes*; Springer, 1998; pp 377−422.

(12) Kilpatrick, P. K. Water-in-crude oil emulsion stabilization: Review and unanswered questions. *Energy Fuels* **2012**, *26*, 4017−4026.

(13) Ese, M.-H.; Sjoblom, J.; Fordedal, H.; Urdahl, O.; Ronningsen, H. P. Ageing of interfacially active components and its effect on emulsion stability as studied by means of high voltage dielectric spectroscopy measurements. *Colloids Surf., A* **1997**, *123*, 225−232.

(14) Yarranton, H. W.; Hussein, H.; Masliyah, J. H. Water-in-hydrocarbon emulsions stabilized by asphaltenes at low concentrations. *J. Colloid Interface Sci.* **2000**, *228*, 52−63.

(15) Verruto, V. J.; Le, R. K.; Kilpatrick, P. K. Adsorption and molecular rearrangement of amphoteric species at oil- water interfaces. *J. Phys. Chem. B* **2009**, *113*, 13788−13799.

(16) Pauchard, V.; Rane, J. P.; Zarkar, S.; Couzis, A.; Banerjee, S. Long-term adsorption kinetics of asphaltenes at the oil-water interface: A random sequential adsorption perspective. *Langmuir* **2014**, *30*, 8381−8390.

(17) Rane, J. P.; Zarkar, S.; Pauchard, V.; Mullins, O. C.; Christie, D.; Andrews, A. B.; Pomerantz, A. E.; Banerjee, S. Applicability of the Langmuir equation of state for asphaltene adsorption at the oil-water interface: Coal-derived, petroleum, and synthetic asphaltenes. *Energy Fuels* **2015**, *29*, 3584−3590.

(18) Qiao, P.; Harbottle, D.; Tchoukov, P.; Masliyah, J.; Sjoblom, J.; Liu, Q.; Xu, Z. Fractionation of asphaltenes in understanding their role in petroleum emulsion stability and fouling. *Energy Fuels* **2017**, *31*, 3330−3337.

(19) Eow, J.; Ghadiri, M. Drop-drop Coalescence in an electric field: The effects of applied electric field and electrode geometry. *Colloids Surf., A* **2003**, *219*, 253−279.

(20) Chiesa, M.; Melheim, J.; Pedersen, A.; Ingebrigtsen, S.; Berg, G. Forces acting on water droplets falling in oil under the influence of an electric field: numerical predictions versus experimental observations. *Eur. J. Mech. B-Fluids* **2006**, *24*, 717−732.

(21) Chiesa, M.; Ingebrigtsen, S.; Melheim, J.; Hemmingsen, P.; Hansen, E.; Hestad, O. Investigation of the role of viscosity on electrocoalescence of water droplets in oil. *Sep. Purif. Technol.* **2006**, *50*, 267−277.

(22) Atten, P. Electrohydrodynamics of dispersed drops of conducting liquid: From drop deformation and interaction to emulsion evolution. *Int. J. Plasma Environ. Sci. Technol.* **2013**, *7*, 2−12.

(23) Yeganeh, M.; Hegner, J.; Lewandowski, E.; Mohan, A.; Lake, L. W.; Cherney, D.; Jusufi, A.; Jaishankar, A. In *Capillary Desaturation Curve Fundamentals*, SPE improved oil recovery conference. Tulsa, Oklahoma, USA, 2016.

(24) Nowbahar, A.; Whitaker, K. A.; Schmitt, A. K.; Kuo, T.-C. Mechanistic study of water droplet coalescence and flocculation in diluted bitumen emulsions with additives using microfluidics. *Energy Fuels* **2017**, *31*, 10555−10565.

(25) Lin, Y.-J.; Perrard, A.; Biswal, S. L.; Hill, R. M.; Trabelsi, S. Microfluidic investigation of asphaltenes-stabilized water-in-oil emulsions. *Energy Fuels* **2018**, *32*, 4903−4910.

(26) Baroud, C. N.; Gallaire, F.; Dangla, R. Dynamics of microfluidic droplets. *Lab Chip* **2010**, *10*, 2032−2045.

(27) Gu, H.; Duits, M.; Mugele, F. Droplets formation and merging in two-phase flow microfluidics. *Int. J. Mol. Sci.* **2011**, *122*, 2572−2597.

(28) Bremond, N.; Bibette, J. Exploring emulsion science with microfluidics. *Soft Matter* **2012**, *8*, 10549.

(29) Huerre, A.; Miralles, V.; Jullien, M. Bubbles and foams in microfluidics. *Soft Matter* **2014**, *10*, 6888−6902.

(30) Theberge, A. B.; Courtois, F.; Schaerli, Y.; Fischlechner, M.; Abell, C.; Hollfelder, F.; Huck, W. T. S. Microdroplets in microfluidics: An evolving platform for discoveries in chemistry and biology. *Angew. Chem., Int. Ed.* **2005**, *49*, 5846−5868.
(31) Urbanski, J. P.; Thies, W.; Rhodes, C.; Amarasinghe, S.; Thorsen, T. Digital microfluidics using soft lithography. *Lab Chip* **2006**, *6*, 96−104.
(32) Huebner, A.; Sharma, S.; Srisa-Art, M.; Hollfelder, F.; Edel, J. B.; deMello, A. J. Microdroplets: A sea of applications. *Lab Chip* **2008**, *8*, 1244−1254.
(33) Teh, S.-Y.; Lin, R.; Hung, L.-H.; Lee, A. P. Droplet microfluidics. *Lab Chip* **2008**, *8*, 198−220.
(34) Chiu, D.; Lorenz, R.; Jeffries, G. Droplets for ultra small-volume analysis. *Anal. Chem.* **2009**, *81*, 5111−5118.
(35) i Solvas, X. C.; deMello, A. Droplet microfluidics: recent developments and future applications. *Chem. Commun.* **2010**, *47*, 1936−1942.
(36) Joensson, H. N.; Andersson-Svahn, H. Droplet microfluidics-a tool for protein engineering and analysis. *Lab Chip* **2011**, *11*, 4144−4147.
(37) Joensson, H. N.; Andersson Svahn, H. Droplet microfluidics a tool for single-cell analysis. *Angew. Chem., Int. Ed.* **2012**, *51*, 12176−12192.
(38) Guo, M. T.; Rotem, A.; Heyman, J. A.; Weitz, D. A. Droplet microfluidics for high-throughput biological assays. *Lab Chip* **2012**, *12*, 2146−2155.
(39) Seemann, R.; Brinkmann, M.; Pfohl, T.; Herminghaus, S. Droplet based microfluidics. *Rep. Prog. Phys.* **2012**, *75*, No. 016601.
(40) Sesen, M.; Alan, T.; Neild, A. Droplet control technologies for microfluidic high throughput screening (micro HTS). *Lab Chip* **2017**, *17*, 2372−2394.
(41) Schwartz, J. A.; Vykoukal, J. V.; Gascoyne, P. R. C. Droplet-based chemistry on a programmable micro-chip. *Lab Chip* **2004**, *4*, 11−17.
(42) Kralj, J.; Schmidt, M.; Jensen, K. Surfactant enhanced liquid-liquid Extraction in microfluidic channels with inline electric field enhanced coalescence. *Lab Chip* **2005**, *5*, 531−535.
(43) Ahn, K.; Agresti, J.; Chong, H.; Marquez, M.; Weitz, D. A. Electrocoalescence of drops synchronized by size-dependent flow in microfluidic channels. *Appl. Phys. Lett.* **2006**, *88*, 264105−3.
(44) Wang, W.; Yang, C.; Li, C. Efficient on-demand compound droplet formation: From microfluidics to microdroplets as miniaturized laboratories. *Small* **2009**, *5*, 1149−1152.
(45) Niu, X.; Gielen, F.; deMello, A. J.; Edel, J. B. Electro-coalescence of digitally controlled droplets. *Anal. Chem.* **2009**, *81*, 7321−7325.
(46) Zagnoni, M.; Cooper, J. M. On-chip electrocoalescence of microdroplets as a function of voltage, frequency and droplet size. *Lab Chip* **2009**, *9*, 2652−2658.
(47) Zagnoni, M.; Lain, G. L.; Cooper, J. Electrocoalescence mechanisms of microdroplets using localized electric fields in microfluidic channels. *Langmuir* **2010**, *26*, 1443−14449.
(48) Gu, H.; Murade, C.; Duits, M.; Mugele, F. A microfluidic platform for on-demand formation and merging of microdroplets Using Electric Control. *Biomicrofluidics* **2011**, *5*, No. 011101.
(49) Chokkalingam, V.; Ma, Y.; Thiele, J.; Schalk, W.; Tei, J.; Huck, W. An Electro-coalescence chip for effective emulsion breaking in droplet microfluidics. *Lab Chip* **2014**, *14*, 2398−2402.
(50) Bhattacharjee, B.; Vanapalli, S. Electrocoalescence based serial dilution of microfluidic droplets. *Biomicrofluidics* **2014**, *8*, No. 044111.
(51) Latham, J.; Roxburgh, I. Disintegration of pairs of water drops in an electric field. *Proc. R. Soc. London, Ser. A* **1966**, *295*, 84−97.
(52) Taylor, G. The coalescence of closely spaced drops when they are at different electric potentials. *Proc. R. Soc. London, Ser. A* **1968**, *306*, 423.
(53) Brazier-Smith, P.; Latham, J. Numerical computations of the dynamics of disintegration of a drop Situated in an Electric Field. *Proc. R. Soc. London, Ser. A* **1969**, *312*, 277−289.
(54) Brazier-Smith, P.; Jennings, S.; Latham, J. An investigation of the behavior of drops and drop-pairs subjected to strong electrical forces. *Proc. R. Soc. London, Ser. A* **1971**, *325*, 363−366.
(55) Atten, P. Electrocoalescence of water drops in an insulating liquid. *J. Electrost.* **1993**, *30*, 259−270.
(56) Zhang, X.; Basaran, O.; Wham, R. Theoretical prediction of electric field enhanced coalescence of spherical drops. *AIChE J.* **1995**, *41*, 1629−1639.
(57) Baygents, J.; Rivette, N.; Stone, H. Electrohydrodynamic Deformation and interaction of drop pairs. *J. Fluid Mech.* **1998**, *368*, 359−375.
(58) Adamiak, K. Interaction of two dielectric or conducting droplets aligned in the uniform electric field. *J. Electrost.* **2001**, *51*, 578−584.
(59) Atten, P.; Lundgaard, L.; Berg, G. A simplified model of electrocoalescence of two close water droplets in oil. *J. Electrost.* **2006**, *64*, 550−554.
(60) Mohammadi, M.; Shahhosseini, S.; Bayat, M. Numerical study of the collision and coalescence of water droplets in an electric field. *Chem. Eng. Technol.* **2014**, *37*, 27−35.
(61) Mohammadi, M. Numerical and experimental study on electric field driven coalescence of binary falling droplets in oil. *Sep. Purif. Technol.* **2017**, *176*, 262−276.
(62) Mhatre, S.; Deshmukh, S.; Thaokar, R. M. Electrocoalescence of a drop pair. *Phys. Fluids* **2015**, *27*, No. 092106.
(63) Bartlett, C. T.; Général, G. A.; Bird, J. C. Coalescence and break-up of nearly inviscid conical droplets. *J. Fluid Mech.* **2015**, *763*, 369−385.
(64) Lu, J.; Fang, S.; Corvalan, C. M. Coalescence dynamics of viscous conical drops. *Phys. Rev. E* **2016**, *93*, No. 023111.
(65) Garzon, M.; Gray, L.; Sethian, J. Electrohydrodynamic coalescence of droplets using an embedded potential flow model. *Phys. Rev. E* **2018**, *97*, No. 033112.
(66) Anand, V.; Roy, S.; Naik, V. M.; Juvekar, V. A.; Thaokar, R. M. Electrocoalescence of a pair of conducting drops in an insulating oil. *J. Fluid Mech.* **2019**, *859*, 839−850.
(67) Anand, V.; Patel, R.; Naik, V. M.; Juvekar, V. A.; Thaokar, R. M. Modelling and particle based simulation of electro-coalescence of a water-in-oil emulsion. *Comput. Chem. Eng.* **2019**, *121*, 608−617.
(68) Zhou, Y.; Dong, H.; Liu, Y.-H.; Yang, Z.-J.; Liu, T.; Li, M. Molecular dynamics simulations of the electrocoalescence behaviors of two unequally sized conducting droplets. *Langmuir* **2019**, *35*, 6578−6584.
(69) Allan, R.; Mason, S. Particle motions in sheared suspensions. XIV. Coalescence of liquid drops in electric and shear fields. *J. Colloid Sci.* **1962**, *17*, 383−408.
(70) Chabert, M.; Dorfman, K.; Viovy, J. Droplet Fusion by Alternating Current (AC) Field Electrocoalescence in microchannels. *Electrophoresis* **2005**, *26*, 3706−3715.
(71) Thiam, A. R.; Bremond, N.; Bibette, J. Breaking of an emulsion under an ac electric field. *Phys. Rev. Lett.* **2009**, *102*, No. 188304.
(72) Priest, C.; Herminghaus, S.; Seemann, R. Controlled electro-coalescence in microfluidics: Targeting a single lamella. *Appl. Phys. Lett.* **2006**, *89*, 134101−3.
(73) Luo, X.; Yin, H.; Yan, H.; Huang, X.; Yang, D.; He, L. The electrocoalescence behavior of surfactant-laden droplet pairs in oil under a DC electric field. *Chem. Eng. Sci.* **2018**, *191*, 350−357.
(74) Luo, X.; Yin, H.; Ren, J.; Yan, H.; Lü, Y.; He, L. Electrocoalescence criterion of conducting droplets suspended in a viscous fluid. *J. Phys. Chem. C* **2019**, *123*, 19588−19595.
(75) Bird, J.; Ristenpart, W.; Belmonte, A.; Stone, H. Critical Angle for Electrically driven coalescence of two conical droplets. *Phys. Rev. Lett.* **2009**, *103*, No. 164502.
(76) Mohammadi, M.; Shahhosseini, S.; Bayat, M. Electro-coalescence of binary water droplets falling in oil: Experimental study. *Chem. Eng. Res. Des.* **2014**, *92*, 2694−2704.
(77) Xia, Y.; Reboud, J.-L. Hydrodynamic and electrostatic interactions of water droplet pairs in oil and electrocoalescence. *Chem. Eng. Res. Des.* **2019**, *144*, 472−482.

https://dx.doi.org/10.1021/acsomega.9b04259
ACS Omega 2020, 5, 7348−7360

(78) Jones, T. B.; Jones, T. B. *Electromechanics of Particles*; Cambridge University Press, 2005.
(79) Pethig, R. Review Article—Dielectrophoresis: Status of the the theory, technology and applications. *Biomicrofluidics* **2010**, *4*, No. 022811.
(80) Kirby, B. J. *Micro-and Nanoscale Fluid Mechanics: Transport in Microfluidic Devices*; Cambridge University Press, 2010.
(81) Pethig, R. R. *Dielectrophoresis: Theory, Methodology and Biological Applications*; John Wiley & Sons, 2017.
(82) Eow, J.; Ghadiri, M.; Sharif, A. Experimental studies of deformation and break-up of aqueous drops in high electric fields. *Colloids Surf., A* **2003**, *225*, 193−210.
(83) Davis, M. H. Two charged spherical conductors in a unifrom electric field: forces and field strength. *Q. J. Mech. Appl. Math.* **1964**, *17*, 499−511.
(84) Taylor, G. Disintegration of water drops in am electric field. *Proc. R. Soc. London, Ser. A* **1964**, *280*, 383−397.
(85) Stone, H.; Lister, J.; Brenner, M. Drops with conical ends in electric and magnetic fields. *Proc. R. Soc. London, Ser. A* **1999**, *455*, 329−347.
(86) Rhodes, A.; Yariv, E. The elongated shape of a dielectric drop deformed by a strong electric field. *J. Fluid Mech.* **2010**, *664*, 286−296.
(87) Ristenpart, W.; Bird, J.; Belmonte, A.; Dollar, F.; Stone, H. Non-Coalescence of oppositely charged drops. *Nat. Lett.* **2009**, *461*, 377−380.
(88) Hamlin, B.; Creasey, J.; Ristenpart, W. Electrically tunable partial coalescence of oppositely charged drops. *Phys. Rev. Lett.* **2012**, *109*, No. 094501.
(89) Raisin, J.; Reboud, J.; Atten, P. Electrically induced deformations of water-air and water-oil interfaces in relation to electrocoalescence. *J. Electrost.* **2011**, *69*, 275−283.
(90) Wang, J.; Wang, B.; Qiu, H. Coalescence and breakup of oppositely charged droplets. *Sci. Rep.* **2014**, *4*, No. 7123.
(91) Liu, Z.; Wyss, H. M.; Fernandez-Nieves, A.; Shum, H. C. Dynamics of oppositely charged emulsion droplets. *Phys. Fluids* **2015**, *27*, No. 082003.
(92) Liu, Z.; Chan, S. T.; Faizi, H. A.; Roberts, R. C.; Shum, H. C. Droplet-based electro-coalescence for probing threshold disjoining pressure. *Lab Chip* **2015**, *15*, 2018−2024.
(93) Anand, V.; Juvekar, V. A.; Thaokar, R. M. Modes of coalescence of aqueous anchored drops in insulating oils under an electric field. *Colloids Surf., A* **2019**, *568*, 294−300.
(94) Chen, X.; Liu, P.; Qi, C.; Wang, T.; Liu, Z.; Kong, T. Non-coalescence of oppositely charged droplets in viscous oils. *Appl. Phys. Lett.* **2019**, *115*, No. 023701.
(95) Szymborski, T.; Korczyk, P.; Holyst, R.; Garstecki, P. Ion Polarization of liquid-liquid interfaces; Dynamic control of the rate of electro-coalescence. *Appl. Phys. Lett.* **2011**, *99*, No. 094101.
(96) Baret, J.-C. Surfactants in droplet-based microfluidics. *Lab Chip* **2011**, *12*, 422−433.
(97) Gaiser, P.; Binz, J.; Gompf, B.; Berrier, A.; Dressel, M. Tuning the dielectric properties of metallic-nanoparticle/elastomer composites by strain. *Nanoscale* **2015**, *7*, 4566−4571.
(98) Saville, D. A. Electrohydrodynamics: The Taylor-Melcher leaky dielectric model. *Annu. Rev. Fluid Mech.* **1997**, *29*, 27−64.
(99) Balinov, B.; Urdahl, O.; Soderman, O.; Sjoblom, J. Characterization of water-in-crude oil emulsions by the NMR self-diffusion technique. *Colloids Surf., A* **1994**, *82*, 173−181.
(100) Hjartnes, T. N.; Mhatre, S.; Gao, B.; Sørland, G. H.; Simon, S.; Sjöblom, J. Demulsification of crude oil emulsions tracked by pulsed field gradient NMR. Part II: Influence of chemical demulsifiers in external AC electric field. *Colloids Surf., A* **2019**, *586*, No. 124188.
(101) Hjartnes, T. N.; Sørland, G. H.; Simon, S.; Sjöblom, J. Demulsification of Crude Oil Emulsions Tracked by Pulsed Field Gradient (PFG) Nuclear Magnetic Resonance (NMR). Part I: chemical demulsification. *Ind. Eng. Chem. Res.* **2019**, *58*, 2310−2323.
(102) McDonald, J. C.; Duffy, D. C.; Anderson, J. R.; Chiu, D. T.; Wu, H. K.; Schueller, O. J. A.; Whitesides, G. M. Fabrication of microfluidic systems in poly(dimethylsiloxane). *Electrophoresis* **2000**, *21*, 27−40.
(103) Urdahl, O.; Wayth, N. I.; Fördedal, H.; Williams, T. J.; Bailey, A. G. *Encyclopedic Handbook of Emulsion Technology*; CRC Press, 2001; pp 678−693.

https://dx.doi.org/10.1021/acsomega.9b04259
ACS Omega 2020, 5, 7348−7360